Article

Polymer-templated gold nanoparticles on optical fibers for enhanced-sensitivity localized surface plasmon resonance biosensors

Mengdi Lu, Hu Zhu, C. Geraldine Bazuin, Wei Peng, and Jean-François Masson

ACS Sens., **Just Accepted Manuscript** • DOI: 10.1021/acssensors.8b01372 • Publication Date (Web): 30 Jan 2019

Polymer-templated gold nanoparticles on optical fibers for enhanced-sensitivity localized surface plasmon resonance biosensors

Mengdi Lu[1,2], Hu Zhu[2], C. Geraldine Bazuin[2], Wei Peng[*,1], Jean-Francois Masson[*,2]

[1]College of Physics and Optoelectronics Engineering, Dalian University of Technology, Dalian 116024, China
[2]Département de chimie and Centre Québécois sur les Matériaux Fonctionnels (CQMF), Université de Montréal, C.P. 6128 Succ. Centre-Ville, Montreal, QC, Canada H3C 3J7

Contact information:

* Corresponding authors: Wei Peng (wpeng@dlut.edu.cn) and Jean-Francois Masson (jf.masson@umontreal.ca)

Abstract

Dense arrays of well-dispersed gold nanoparticles (AuNPs) on optical fibers are shown to bridge the gap in sensitivity and sensing performance between localized surface plasmon resonance (LSPR) and classical SPR sensing. A simple self-assembly method relying on a poly(styrene-b-4-vinylpyridine) (PS-b-P4VP) block copolymer brush layer was used to immobilize AuNPs of different diameters from 10 to 92 nm on optical fibers. In comparison with standard AuNP deposition methods using (3-aminopropyl)trimethoxysilane (APTMS) and polyelectrolytes, the sensitivity with the PS-b-P4VP templating method was found to be 3-fold better, a consequence of the smaller gap between particles and the presence of fewer AuNP aggregates. Hence, the sensitivity of the LSPR sensor for IgG was comparable to a classical SPR, also on optical fibers, and about 68% of that for a prism-based wavelength-interrogation SPR instrument. The reproducibility and the detection limit of the LSPR sensor were about the same as the SPR sensor. The enhanced performance of the LSPR sensors using the PS-b-P4VP block copolymer fabrication method paves the way for

use of these LSPR biosensors in a smaller and more cost-effective platform.

Keywords: Localized surface plasmon resonance, Optical fiber, biosensor, gold nanoparticle, block copolymer

Sensors based on classical surface plasmon resonance (SPR) and on localized surface plasmon resonance (LSPR) with colloidal gold nanoparticles (AuNPs) or nanostructured metallic films have been increasingly applied in clinical sensing[1]. SPR sensing is most often performed on larger-scale instruments confined to laboratories. Classical SPR instruments can be designed to be portable for clinical applications [2], but LSPR sensing holds the promise of simpler instrumentation [3, 4]. However, it may be costly and complex to fabricate some of the nanostructured substrates necessary for highly sensitive LSPR sensing. In order to provide a simple and low-cost alternative to classical SPR and LSPR sensors, SPR on optical fibers is an interesting option for sensing biomolecules[5-11]. LSPR sensors based on optical fibers and metallic nanoparticle arrays are thus increasingly used in monitoring the refractive index variation in the surrounding medium[12-14] and for biological sensing[15, 16], as shown with biotin-streptavidin[17] and antigen-antibody interactions[18-20]. However, despite significant progress in recent years, the performance of fiber-optic LSPR sensors remains inferior to classical SPR sensors.

The properties of plasmonic sensors fabricated with nanoparticle arrays strongly depends on the size, shape and charge of the metallic nanoparticles, which all influence the strength of the local electric field[21]. The control of these parameters is important for improving sensitivity in the development of new plasmonic sensing technologies[22-24]. In sensor design, AuNPs are usually deposited on a substrate. For this process, there are additional factors that need to be considered in the fabrication of the plasmonic substrates.

For example, the charge of the adhesion layer on the substrate is essential to the assembly process of the nanoparticles[25-27]. The spacing between nanoparticles has been identified early on as one of the main factors influencing the plasmonic properties of arrays[28]. Control of the interparticle spacing of nanoparticle arrays can be achieved among other methods by using a polymer additive in the deposition solution, a method that was shown to be effective for methotrexate and testosterone sensing with a sensitivity approaching that of classical SPR sensors[29, 30].

The fabrication of dense arrays of well-dispersed metallic nanoparticles is crucial for the performance of plasmonic sensors based on nanoparticle arrays. The preparation of metal nanoparticles-based optical fiber LSPR sensors mainly rely on positively charged silane as an electrostatic linking agent to assemble negatively charged nanoparticles[31-36]. This method requires precise control of the immersion temperature and particle assembly time leading, oftentimes, to the fabrication of surfaces with low nanoparticle coverage and the presence of a large number of aggregates[37, 38]. A polyelectrolyte assembly method was thus proposed to simplify the preparation of the optical fiber LSPR sensors[39-41]. A trilayer polyelectrolyte structure served as a linker for the assembly of nanoparticles, with the benefit of greatly reducing the fabrication time compared with the silane method[37, 42]. The sensitivity for polyelectrolyte-based sensors was expected to be improved with the higher coverage of nanoparticles. However, this polyelectrolyte method led to the presence of aggregates at higher nanoparticle coverage, which is detrimental to the plasmonic properties of the LSPR sensor. Specifically, the aggregation of nanoparticles broadens the LSPR band and decreases its intensity, strongly affecting the refractive index resolution, sensitivity and reproducibility of the LSPR sensors[27].

The use of amphiphilic block copolymers (BCs) is another solution of interest for

patterning AuNPs on substrates. Due to block incompatibility, they can self-assemble with a range of morphologies in thin films on surfaces[43-45]. These give rise to uniform arrays of nanoscopic surface structures or patterns that can selectively guide the adsorption of high-density arrays of inorganic nanoparticles[46-50], including AuNPs. However, if the substrates are dipped in very dilute BC solutions, only a uniform nanothin brush-type BC film is formed, where one block adsorbs to the surface as a wetting layer and the other forms a brushlike overlayer. (*unpublished work*) We recently found, using poly(styrene-b-4-vinylpyridine) (PS-b-P4VP) and silicon substrates, that these films function very well as templates, which we term block copolymer brush templates (BCBTs), for fabricating dense and well-dispersed citrate-capped AuNP monolayers with little aggregation[51]. Here, we apply this methodology to the fabrication of fiber-optic LSPR sensors for protein detection and show that it leads to significant gains in sensitivity and sensor performance.

Experimental Section

Materials

$HAuCl_4 \cdot 3H_2O$, trisodium citrate, (3-aminopropyl)trimethoxysilane (APTMS), poly(diallyldimethylammonium chloride) (PDDA, 20 wt% in water, 150 kDa), poly(allylamine) (PAH, 10 wt% in water, 65 kDa), poly(4-styrenesulfonic acid) (PSS, 18 wt% in water, 65 kDa), 11-mercaptoundecanoic acid (11-MUA), ethanol, methanol, chloroform, tetrahydrofuran (THF), phosphate buffer (PBS, pH 7.4), 1-ethyl-3-(3-dimethylaminopropyl)carbodiimide hydrochloride (EDC), N-hydroxysuccinimide (NHS), and bovine serum albumin (BSA) were purchased from Sigma-Aldrich. PS-b-P4VP [M_n(PS) = 41 kg/mol, M_n(P4VP) = 20 kg/mol, M_w/M_n (total) = 1.18] was obtained from Polymer Source. Human gamma globulin (IgG) and affinipure goat anti-human IgG (H+L) were purchased from Cedarlane Labs (Canada). Ultrapure water was used throughout the experiments.

Preparation of optical fibers

Plastic cladded silica multimode optical fibers (HPOF, HP 400/430-37/730E, YOFC Inc., Wuhan, China) were employed in this work. The diameters of the fiber core and with cladding were 400 and 430 μm, respectively, and the numerical aperture was 0.37. The fiber was cut into 10-cm-long sections and a 5-mm unclad portion was exposed in the middle of the fiber as a sensing area. To reduce connection losses, both end faces of the fiber were polished using emery paper. The 5-mm unclad portion was then cleaned and hydrolyzed with Piranha solution (with a volume ratio of 3:1 of H_2SO_4:H_2O_2; *Caution! Piranha solution is highly corrosive*) for 20 min. Following that, the fiber was rinsed with ultrapure water. The fibers were then dried in a room temperature vacuum oven for 20 min.

Preparation of AuNP-based sensing films

The Au colloids were synthesized via the seeded growth method[52]. The AuNPs were grown by adjusting both the seed particle concentration and the total amount of gold atoms in the solution. After synthesis, Au colloids of different sizes (the particles size were determined by UV-vis, as shown in Supporting Information) were centrifuged and redistributed in ultrapure water and the pH was adjusted to 5.0.

For the APTMS templating method, clean fibers were first immersed in a 10% solution of APTMS in methanol for 2 h at 40℃. The fibers were rinsed with ethanol and ultrapure water to remove unbound APTMS, and then dried in the vacuum oven for 20 min. After that, the functionalized fibers were dipped into an AuNP suspension (0.5 nM) for 4 h, then cleaned with ultrapure water and stored in a vacuum oven before use.

For the polyelectrolyte templating method, clean fibers were modified with a layer-by-layer deposition procedure. Three polyelectrolyte solutions were prepared: 0.5% of PDDA, 1 mg/mL of PSS and 1 mg/mL of PAH, which were then successively deposited for 15 min each and the fibers were rinsed by ultrapure water before and after each step. The functionalized fibers were dipped into an AuNP solution for 4 h and stored in the vacuum oven before use.

For the PS-b-P4VP templating method, the cleaned fibers were dipped for 10 min in 0.05 mg/mL solutions of PS-b-P4VP in THF. The fibers were then washed with THF and dipped into an AuNP solution for 4 h. The fibers were rinsed again with ultrapure water and placed in the oven for 20 min. They were finally treated with an oxygen plasma for 1 min at medium power (9 W) in a plasma cleaner (Model PDC-32G from Harrick Plasma) to remove the polymer template.

LSPR measurements

The transmission measurements of the plasmon resonances were performed using a fiber-coupled spectrophotometer (Ocean Optics, HR4000) with an Ocean optics HL-2000 light source. The fiber-optic LSPR sensor was mounted inside a fluidic cell. The refractive index samples were prepared with an aqueous sucrose solution, and RIs were measured with an Abbe refractometer. Spectra were collected from 450 to 850 nm, and data were acquired and processed in real time with Labview software (Fig. 1). Prism-based SPR measurements were done on a P4SPR from Affinité instruments[52]. The error bars were determined from five identically prepared fiber-optic LSPR sensors, and these sensors were obtained from the same batch in order to guarantee the experimental accuracy. The particle size were determined with UV-Vis as shown in Supplementary Information.

Numerical simulations

Simulations of extinction spectra were conducted using FDTD Solutions software (Lumerical Solutions) to correlate experimental data with predicted properties of the AuNP arrays. To perform the calculations, a simplified Kretschmann model[23] with gold nanoparticle arrays was used. The structure used for the simulations is shown in Figure S1. The reflection spectra were simulated at a fixed incident angle of 82°. The model consisted of hexagonal arrays of AuNPs on silica glass (RI = 1.46), where the diameter of the particles and the gap between particles were varied in accordance with the optical fibers experimentally prepared.

Biosensing experiments

The functionalized fiber optics LSPR sensors were immersed in a 10 mM 11-MUA ethanol solution for 12 h to create a monolayer with carboxyl groups on the surface of the AuNPs exposed to the solution. Then, the sensors were rinsed with ethanol and PBS to remove unbound 11-MUA. After that, the sensors were immersed into a solution of 2 mM EDC and 4 mM NHS in water with a volume ratio of 1:1 for 15 min to activate the carboxyl group of 11-MUA. After activation, the sensors were immersed sequentially in a 100 μg/mL anti-human IgG PBS solution for 1 h and in a 1 mg/mL BSA solution in PBS for 1 h to suppress nonspecific binding. The sensors were rinsed with PBS before the next step and stored in a PBS buffer at 4℃ before use. To detect human IgG with the anti-human IgG on the fiber surface, the reflection spectrum was monitored in real time to track the changes in resonance wavelength and intensity. Different concentrations of human IgG were prepared (6.7 to 666.7 nM) and injected sequentially for 30 min each. The PBS buffer was also injected before and after each step. The whole detection process was repeated five times on the same batch of the fiber optics LSPR sensors to determine the reproducibility.

Results and discussion

The fiber optics LSPR sensing system used is simple (Figure 1). Briefly, the AuNP-coated optical fiber was connected to multimode fibers. The light beam illuminated the sensing fiber where it underwent total internal reflection. The evanescent field excited the plasmon resonance of the AuNPs. The fabrication process of the LSPR sensors relied on the interaction of glass-P4VP-AuNPs (Figure 1). Because of the multiple hydrogen bonding sites between P4VP and the glass surface of the optical fiber, the PS-b-P4VP brush layer was very stable and uniform. While the deposition of AuNPs was driven by electrostatic interactions between the AuNPs and protonated P4VP chains, the aggregation of AuNPs appears to be prevented by the presence of the hydrophobic PS blocks. (*unpublished work*) The pH value of the Au colloids was adjusted to 5.0, close to the pKa of pyridine groups of P4VP, to favor the electrostatic interactions. In acidic solutions, most of the pyridine groups in P4VP were protonated, providing a positive surface charge, opposite to the negative charge of the AuNPs. This results in a dense but well-dispersed monolayer of AuNPs on the optical fibers.

Refractive index sensitivity of the fiber optics LSPR sensor

Arrays of AuNPs with different diameters were self-assembled on the PS-b-P4VP brush layer on the optical fiber. The optical properties of these fibers were measured in total internal reflection guided by the optical fiber (Figure 2 - see also the 2D spectra in Figure S2). The absorption spectrum for the LSPR sensor with 10-nm AuNPs on the fiber optics were measured in water and it revealed an absorption band centered at 553 nm (black line in Figure 2(a)), which is moderately redshifted by 33 nm (Table 1) from the UV-visible spectrum of the aqueous colloidal suspension (Figure S3) due to the higher refractive index of glass compared to water. As the AuNP diameter increased, the plasmon resonance varied from 553 to 715 nm, and the difference in plasmon resonance between the AuNPs in

colloidal suspension and self-assembled on the optical fiber increased to as much as 155 nm for the largest AuNPs (Table 1). The full width at half maximum (FWHM) of the plasmon resonance for AuNPs self-assembled on the fiber is narrow at nearly 60 nm for diameters of 10 to 54 nm, but increases by up to a factor of 2 for larger AuNPs. The intensity of the plasmon resonance, measured as the % depth, increases with particle diameter up to 54 nm, and slightly decreased for larger diameters. Hence, 54-nm AuNPs offered the optimal optical properties on the fibers.

To investigate refractive index sensitivity of the plasmon resonance for different AuNP sizes, the absorption spectra in solution of different sucrose concentrations (causing the refractive index to vary from 1.33 to 1.35) were recorded. The refractive index resolution for our fiber-based sensor system was measured to be 4.6 x 10^{-4} RIU. The plasmon resonance red-shifted and the intensity increased linearly with refractive index. The sensitivity was measured by the plasmon resonance shift and by the intensity change as a function of AuNP sizes (Figures 2(b) and 2(c), respectively). The maximum refractive index sensitivity was measured at 570%/RIU from the intensity change of the plasmon resonance of 42-nm AuNPs (Figure 2(c)). The refractive index sensitivity measured from the plasmon resonance wavelength increased from 84 to 1079 nm/RIU with larger AuNP diameters.

Our results present a stark increase in refractive index sensitivity compared to AuNPs in suspension. Refractive index sensitivity is usually on the order of 40 to 180 nm/RIU for suspensions of spherical AuNPs of 15 nm[53] to 100 nm[54] in diameter. One could think that the effect of adsorbing the metallic nanoparticles on a solid substrate may lead to an increase in sensitivity. For example, Ag nanocubes[55, 56] and Ag spheres were previously found to have a slight decrease in refractive index sensitivity on glass. Au nanodisks on a

glass substrate revealed an ambiguous behavior, where the shift magnitude could be adjusted with the incident angle in total internal reflection measurements[56]. However, these literature results do not show any stark difference in sensitivity and therefore do not explain the high increase in the peak wavelength sensitivity we observed. We therefore investigated this behavior with FDTD simulations (see Supporting Information). These simulations indicate that hexagonal arrays of AuNPs on glass also exhibited high sensitivity. Hence, we conclude that the pseudo-hexagonal ordering of the AuNPs on the PS-b-P4VP templated fiber contributes to the enhanced sensitivity of the LSPR sensors reported here.

FDTD simulations were also performed to estimate the penetration depth of the plasmon field with different particle diameters and interparticle gaps. The penetration depth at the plasmon resonance wavelength was first modeled as a function of the interparticle gap, with AuNPs of 31 nm diameter. The penetration depth exponentially decayed with larger gaps, from about 100 nm penetration depth for short gap distances to 20-30 nm at longer gap distances (Figure 3(a)). These results agree to the ones shown by Jain and El-Sayed. Compared with the results in Fig. S4(a), the decreased penetration depth lead to a smaller refractive index sensitivity. The penetration depth was also calculated for different AuNP diameters with a constant interparticle gap of 60 nm (Figure 3(b)). In this case, the penetration depth increased from about 20-30 nm to nearly 200 nm with the particle diameter. The longer penetration depth of the larger particles is not far from the ones of a flat Au film, which is nearly 230 nm. We also noted that higher refractive index sensitivity was obtained with AuNPs of larger diameter (Fig. 4S(b)).”

To evaluate the performance of the AuNP arrays fabricated with the PS-b-P4VP template, they were compared with those fabricated by two common templating methods (APTMS and PDDA/PSS/PAH). AuNPs with a diameter of 31 nm was used for the comparison, since particles of this size have been widely reported for LSPR fiber sensors. Figure 4 shows the scanning electron microscopy (SEM) images of the AuNP films made

with the three fabrication methods. The distribution of the AuNPs on the PS-b-P4VP template was generally dense and well dispersed, but the APTMS and PDDA/PSS/PAH methods led to a high fraction of AuNP aggregates and uneven distribution. Clearly, the PS-b-P4VP brush layer played an important role in the AuNP self-assembly to drastically reduce the aggregation. It also increased the surface coverage of the AuNPs, determined to be 18.3 ± 0.3% compared to 12.2 ± 0.4% with the APTMS film and 15.5 ± 0.8% with the polyelectrolyte multilayer. The average interparticle spacing of the AuNPs for PS-b-P4VP brush layer was calculated with Engineer's Toolbox (https://www.engineeringtoolbox.com/circles-within-rectangle-d_1905.html). We assumed a pseudo-hexagonal order for all templates, which is a better assumption for the PS-b-P4VP film than for the APTMS and polyelectrolyte films where more randomness in orientation was observed. It was found out that the interparticle spacing was 75 ± 13 nm for the PS-b-P4VP film, lower than 102 ± 21 nm with the APTMS film and 109 ± 19 nm with the polyelectrolyte multilayer. Hence, the PS-b-P4VP brush layer facilitated the fabrication of denser arrays of closely packed AuNPs.

The sensitivity of the resonance wavelength shift and intensity change was also compared for the three AuNP deposition methods on the optical fibers (Figure 4(d)) and was found to be significantly better for the PS-b-P4VP templating method. The sensitivity measured from the intensity change for the PS-b-P4VP templated AuNPs was 440%/RIU, compared to 270%/RIU for APTMS and 290%/RIU for the polyelectrolyte multilayer. The difference in resonance wavelength sensitivity is even more striking. The PS-b-P4VP templated AuNPs has a sensitivity of 326 nm/RIU, about 3-fold better than APTMS (109 nm/RIU) and the polyelectrolyte multilayer (112 nm/RIU) methods. These results illustrated that aggregation, random orientation and the lower coverage of AuNPs decreased the sensitivity to refractive index of both the resonance shift and intensity change, more significantly for resonance shift. Hence, we conclude that the gain in sensitivity

observed from the AuNPs templated with PS-b-P4VP is from the higher degree of ordering and the formation of a denser layer.

The effect of diameter of particles and gap between particles

AuNP geometrical effects using the PS-b-P4VP templating method were further investigated with a series of SEM images for different AuNP diameters (Figure 5). The factors affecting the particle coverage were the repulsive forces between particles and the attraction between the particles and the optical fiber surface[37]. The AuNPs were well dispersed on the fiber surface with little aggregation for all diameters.

Two characteristic features were assessed in the SEM images: (i) the AuNP coverage and (ii) the gap between particles (Figure 6). The coverage was measured as the percentage area covered with AuNPs (S_{Au}) in an area of 1 x 1 μm. Different sizes of AuNPs had approximately the same coverage value at 19%, except for the 92-nm AuNPs, which was lower in agreement with its lower density. The interparticle gaps (the interparticle gap is the distance between the edges of neighboring particles) and periodicities were determined assuming hexagonal AuNP arrays, and were found to increase with AuNP diameter from 28 to 90 nm (Figure 6(b)). In addition, the gap/diameter ratio decreased significantly from 2.80 to 1.64, 1.42, 1.21, 1.14, 1.01, and 0.98 with increase in particle size from 10 to 92 nm. In this connection, it was observed that the smaller gap/diameter ratio for larger particles exhibited stronger plasmonic coupling, which led to a larger plasmon resonance wavelength and higher sensitivity. These results are in good agreement with the simulation results provided in the Supporting Information and Figure S4.

IgG biosensing with different sensor constructions

The optical fiber modified with 31-nm AuNPs using the three deposition methods (PS-b-P4VP, APTMS and PDDA/PSS/PAH) were employed for protein biosensing with the detection of human IgG with anti-human IgG immobilized on the AuNPs. The calibration curves for human IgG followed the expected Langmuir isotherm (Figure 7(a)). The AuNPs on a PS-b-P4VP template performed better compared with fiber sensors based on APTMS and PDDA/PSS/PAH. For example, when the concentration of human IgG was 667 nM, the peak wavelength shift of PS-b-P4VP brush layer- based sensor was about 5 times higher than that of AuNPs on APTMS and 2 times higher than that of AuNPs on PDDA/PSS/PAH.

To better illustrate the effectiveness of the PS-b-P4VP brush layer-based sensor, calibration curves are shown for a range of low concentrations of human IgG (6.7-66.7 nM). To quantitatively evaluate the biosensing performance of the LSPR sensor, we analyzed the limit of detection (LOD) of human IgG samples. It was calculated from the concentration of human IgG sample that resulted in a response of 3 times the noise level and defined to be the standard deviation of replicate measurements on 5 blank samples. This yielded an LOD of 1.2 nM for the PS-b-P4VP-templated AuNPs. Comparatively, the LODs for APTMS and PDDA/PSS/PAH were 37 nM and 3.4 nM, respectively. Similar results were obtained from the peak intensity shifts, where the LODs were 6.8 nM, 3.0 nM and 1.1 nM for APTMS, PDDA/PSS/PAH and PS-b-P4VP templates, respectively. Overall, the peak intensity was more sensitive than the peak wavelength for lower concentration biosensing. However, the difference in LOD between intensity and wavelength was very small for the PS-b-P4VP brush layer-based sensor. This might be due to the dense and unaggregated AuNP arrays on the sensing area, leading to a much more stable and sensitive biosensor. The peak wavelength and intensity shifts were then compared with human IgG (66.7 nM) for different AuNP diameters (31, 54 and 76 nm) using the PS-b-P4VP template (Figure 8(a)). Both peak wavelength and intensity shifts increased with increase in particle diameter. In particular, the responses of the 76-nm AuNPs were found to be 2-fold better

than the 31-nm AuNPs.

Finally, we compared the sensitivity of the fiber-optic LSPR sensor to a classical SPR sensor. Calibration curves for IgG sensing were constructed for both prism-based and fiber-based types of sensors (Figure 8(b)). The thickness of the gold film for SPR was 45 nm, and the AuNP diameter for LSPR was 76 nm. The change of magnitude in the response to 667 nM IgG for these sensors were close, as only a small decrease of 17% (prism-based SPR) or 32% (fiber-based SPR) was observed in the response magnitude of the LSPR sensor. Reproducibility was nearly the same, with relative errors of 5%, 6%, and 7% for the prism-based SPR, fiber-based SPR, and LSPR sensors, respectively. The LOD was also similar, measured to be 0.3 nM, 0.4 nM, and 0.8 nM for the prism-based SPR, fiber-based SPR, and LSPR sensors, respectively.

Finally, we evaluated the surface coverage for the highest concentration of IgG detected and calculated a relative sensitivity with the different templates to prepare the LSPR sensors. The sensitivity expressed in SPR shift (in nm) per surface concentration unit (in ng/cm^2) was used for comparison of the magnitude of the response for a constant number of molecules detected. The surface coverage of IgG was lowest at 26 ng/cm^2 for APTMS, and increased for the PDDA/PSS/PAH sensor (71 ng/cm^2), PS-b-P4VP (76 ng/cm^2) and for the flat film (153 ng/cm^2). When corrected for the intensity of the SPR response, we observed that the APTMS and PDDA/PSS/PAH templates had the same sensitivity at 0.020 nm/(ng/cm^2) and the PS-b-P4VP and flat films had nearly identical sensitivities of 0.036 and 0.038 nm/(ng/cm^2), respectively. Hence, the PS-b-P4VP template resulted in a similar SPR shift for the same number of molecules as the classical flat gold film. The results presented here demonstrate that the use of the PS-b-P4VP brush-layer template to deposit AuNPs on optical fibers closes the gap in performance between LSPR and SPR sensors.

Conclusions

In summary, we demonstrated an optical fiber-based biosensor that exploited the increased sensitivity of self-assembled Au colloids on a PS-b-P4VP brush template for refractive index sensing and for protein immunoassays. Studies presented in this paper illustrated the feasibility of fabricating optical fibers modified with colloidal AuNPs of various sizes for chemical and biochemical sensing. By comparing the performances of different self-assembly methods, we showed that the PS-b-P4VP brush template demonstrated dense and well-dispersed AuNP adsorption and high sensitivity for LSPR sensing. Furthermore, the results suggested that the particle size, particle coverage and the interparticle gap were important factors affecting the optical properties of fiber-based LSPR sensors. The largest nanoparticles showed greater peak wavelength sensitivities; however, nanoparticles of intermediate size (42 nm) gave higher peak intensity sensitivities. With decreasing interparticle gap, the peak wavelength red-shifted and the wavelength sensitivity increased. The sensitivity of the sensor was useful for biosensor applications, and the low detection limit of the sensor for human IgG was 1.1 nM. Compared with other LSPR sensors, the PS-b-P4VP based fiber sensor showed great potential for biomolecule detection in practical applications. Thus, this study is a significant step forward for the development of a simple and efficient optical fiber LSPR sensor.

Associated content

Supporting Information Available: The following files are available free of charge.

File name. FDTD simulations; FDTD model and simulations of the plasmon resonance wavelength and sensitivity, UV-vis spectra of AuNPs on optical fibers.

Acknowledgements

We acknowledge funding from the Natural Science and Engineering Research Council (NSERC) of Canada (Grant RGPIN-2016-03864), the Fonds de Recherche du Québec—Nature et Technologies (FRQ-NT) (Grant 205260), the National Nature Science Foundation of China (NSFC) (Grant Nos. 61727816, 61520106013, and 11474043) and support from the China Scholarship Council (CSC).

Disclosure

Jean-Francois Masson has financial interest in Affinité Instruments.

References

1. Masson, J. F., Surface Plasmon Resonance Clinical Biosensors for Medical Diagnostics. *ACS Sensors* 2017, 2, 16-30.

2. Zhao, S. S.; Bukar, N.; Toulouse, J. L.; Pelechacz, D.; Robitaille, R.; Pelletier, J. N.; Masson, J.-F., Miniature multi-channel SPR instrument for methotrexate monitoring in clinical samples. *Biosensors & Bioelectronics* 2015, 64, 664-670.

3. Dutta, S.; Saikia, K.; Nath, P., Smartphone based LSPR sensing platform for bio-conjugation detection and quantification. *RSC Advances* 2016, 6, 21871-21880.

4. Zhang, D.; Liu, Q., Biosensors and bioelectronics on smartphone for portable biochemical detection. *Biosensors and Bioelectronics* 2016, 75, 273-284.

5. Caucheteur, C.; Guo, T.; Albert, J., Review of plasmonic fiber optic biochemical sensors: improving the limit of detection. *Analytical and Bioanalytical Chemistry* 2015, 407, 3883-3897.

6. Masson, J. F.; Obando, L.; Beaudoin, S.; Booksh, K., Sensitive and real-time fiber-optic-based surface plasmon resonance sensors for myoglobin and cardiac troponin I. *Talanta* 2004, 62, 865-870.

7. Piliarik, M.; Homola, J.; Manikova, Z.; Ctyroky, J., Surface plasmon resonance sensor based on a single-mode polarization-maintaining optical fiber. *Sensors and Actuators B-Chemical* 2003, 90, 236-242.

8. Pollet, J.; Delport, F.; Janssen, K. P. F.; Jans, K.; Maes, G.; Pfeiffer, H.; Wevers, M.; Lammertyn, J., Fiber optic SPR biosensing of DNA hybridization and DNA-protein interactions. *Biosensors & Bioelectronics* 2009, 25, 864-869.

9. Sai, V. V. R.; Kundu, T.; Mukherji, S., Novel U-bent fiber optic probe for localized surface plasmon resonance based biosensor. *Biosensors & Bioelectronics* 2009, 24, 2804-2809.

10. Sharma, A. K.; Jha, R.; Gupta, B. D., Fiber-optic sensors based on surface plasmon resonance: A comprehensive review. *Ieee Sensors Journal* 2007, 7, 1118-1129.

11. Slavik, R.; Homola, J.; Brynda, E., A miniature fiber optic surface plasmon resonance sensor for fast detection of staphylococcal enterotoxin B. *Biosensors & Bioelectronics* 2002, 17, 591-595.

12. Chung, T.; Lee, S.-Y.; Song, E. Y.; Chun, H.; Lee, B., Plasmonic nanostructures for nano-scale bio-sensing. *Sensors* 2011, 11, 10907-10929.

13. Murray, W. A.; Suckling, J. R.; Barnes, W. L., Overlayers on silver nanotriangles: field confinement and spectral position of localized surface plasmon resonances. *Nano letters* 2006, 6, 1772-1777.

14. Jin, R.; Cao, Y. C.; Hao, E.; Métraux, G. S.; Schatz, G. C.; Mirkin, C. A., Controlling anisotropic nanoparticle growth through plasmon excitation. *Nature* 2003, 425, 487-490.

15. Cao, J.; Tu, M. H.; Sun, T.; Grattan, K. T., Wavelength-based localized surface plasmon resonance optical fiber biosensor. *Sensors and Actuators B: Chemical* 2013, 181, 611-619.

16. Fan, M.; Thompson, M.; Andrade, M. L.; Brolo, A. G., Silver nanoparticles on a plastic platform for localized surface plasmon resonance biosensing. *Analytical chemistry* 2010, 82, 6350-6352.

17. Wan, M.; Luo, P.; Jin, J.; Xing, J.; Wang, Z.; Wong, S. T., Fabrication of localized surface plasmon resonance fiber probes using ionic self-assembled gold nanoparticles. *Sensors* 2010, 10, 6477-6487.

18. Kim, H. M.; Jin, S. M.; Lee, S. K.; Kim, M.-G.; Shin, Y.-B., Detection of biomolecular binding through enhancement of localized surface plasmon resonance (LSPR) by gold nanoparticles. *Sensors* 2009, 9, 2334-2344.

19. Oldenburg, S.; Averitt, R.; Westcott, S.; Halas, N., Nanoengineering of optical resonances. *Chemical Physics Letters* 1998, 288, 243-247.

20. Liang, G.; Zhao, Z.; Wei, Y.; Liu, K.; Hou, W.; Duan, Y., Plasma enhanced label-free immunoassay for alpha-fetoprotein based on a U-bend fiber-optic LSPR biosensor. *RSC Advances* 2015, 5, 23990-23998.

21. Yockell-Lelievre, H.; Lussier, F.; Masson, J. F., Influence of the Particle Shape and

Density of Self-Assembled Gold Nanoparticle Sensors on LSPR and SERS. *Journal of Physical Chemistry C* 2015, 119, 28577-28585.

22. Abe, M.; Suwa, T., Surface plasma resonance and magneto-optical enhancement in composites containing multicore-shell structured nanoparticles. *Physical Review B* 2004, 70, 235103. **DOI:** 10.1103/PhysRevB.70.235103

23. Chen, H.; Kou, X.; Yang, Z.; Ni, W.; Wang, J., Shape-and size-dependent refractive index sensitivity of gold nanoparticles. *Langmuir* 2008, 24, 5233-5237.

24. Haes, A. J.; Van Duyne, R. P., A unified view of propagating and localized surface plasmon resonance biosensors. *Analytical and bioanalytical chemistry* 2004, 379, 920-930.

25. Hsu, C.-Y.; Huang, J.-W.; Lin, K.-J., High sensitivity and selectivity of human antibody attachment at the interstices between substrate-bound gold nanoparticles. *Chemical Communications* 2011, 47, 872-874.

26. Zhang, Q.; Xue, C.; Yuan, Y.; Lee, J.; Sun, D.; Xiong, J., Fiber surface modification technology for fiber-optic localized surface plasmon resonance biosensors. *Sensors* 2012, 12, 2729-2741.

27. Daniel, M.-C.; Astruc, D., Gold nanoparticles: assembly, supramolecular chemistry, quantum-size-related properties, and applications toward biology, catalysis, and nanotechnology. *Chemical reviews* 2004, 104, 293-346.

28. Jain, P. K.; Huang, W.; El-Sayed, M. A., On the Universal Scaling Behavior of the Distance Decay of Plasmon Coupling in Metal Nanoparticle Pairs: A Plasmon Ruler Equation. *Nano Letters* 2007, 7, 2080-2088.

29. Yockell-Lelievre, H.; Bukar, N.; McKeating, K. S.; Arnaud, M.; Cosin, P.; Guo, Y.; Dupret-Carruel, J.; Mougin, B.; Masson, J. F., Plasmonic sensors for the competitive detection of testosterone. *Analyst* 2015, 140, 5105-5111.

30. Yockell-Lelievre, H.; Bukar, N.; Toulouse, J. L.; Pelletier, J. N.; Masson, J. F., Naked-eye nanobiosensor for therapeutic drug monitoring of methotrexate. *Analyst* 2016, 141, 697-703.

31. Mayer, K. M.; Lee, S.; Liao, H.; Rostro, B. C.; Fuentes, A.; Scully, P. T.; Nehl, C. L.; Hafner, J. H., A label-free immunoassay based upon localized surface plasmon resonance of gold nanorods. *ACS nano* 2008, 2, 687-692.

32. Mayer, K. M.; Hafner, J. H., Localized surface plasmon resonance sensors. *Chemical reviews* 2011, 111, 3828-3857.

33. Mitsui, K.; Handa, Y.; Kajikawa, K., Optical fiber affinity biosensor based on localized surface plasmon resonance. *Applied Physics Letters* 2004, 85, 4231-4233.

34. Chau, L.-K.; Lin, Y.-F.; Cheng, S.-F.; Lin, T.-J., Fiber-optic chemical and biochemical probes based on localized surface plasmon resonance. *Sensors and Actuators B: Chemical*

2006, 113, 100-105.

35. Cheng, S.-F.; Chau, L.-K., Colloidal gold-modified optical fiber for chemical and biochemical sensing. *Analytical chemistry* 2003, 75, 16-21.

36. Chen, J.; Shi, S.; Su, R.; Qi, W.; Huang, R.; Wang, M.; Wang, L.; He, Z., Optimization and application of reflective LSPR optical fiber biosensors based on silver nanoparticles. *Sensors* 2015, 15, 12205-12217.

37. Grabar, K. C.; Smith, P. C.; Musick, M. D.; Davis, J. A.; Walter, D. G.; Jackson, M. A.; Guthrie, A. P.; Natan, M. J., Kinetic control of interparticle spacing in Au colloid-based surfaces: rational nanometer-scale architecture. *Journal of the American Chemical Society* 1996, 118, 1148-1153.

38. Freeman, R. G.; Grabar, K. C.; Allison, K. J.; Bright, R. M.; Davis, J. A.; Guthrie, A. P.; Hommer, M. B.; Jackson, M. A.; Smith, P. C.; Walter, D. G., Self-assembled metal colloid monolayers: an approach to SERS substrates. *Science* 1995, 267, 1629-1632.

39. Shao, Y.; Xu, S.; Zheng, X.; Wang, Y.; Xu, W., Optical fiber LSPR biosensor prepared by gold nanoparticle assembly on polyelectrolyte multilayer. *Sensors* 2010, 10, 3585-3596.

40. Liu, G.; Zou, S.; Fu, L.; Zhang, G., Roles of chain conformation and interpenetration in the growth of a polyelectrolyte multilayer. *The Journal of Physical Chemistry B* 2008, 112, 4167-4171.

41. Zhao, W. B.; Park, J.; Caminade, A.-M.; Jeong, S.-J.; Jang, Y. H.; Kim, S. O.; Majoral, J.-P.; Cho, J.; Kim, D. H., Localized surface plasmon resonance coupling in Au nanoparticles/phosphorus dendrimer multilayer thin films fabricated by layer-by-layer self-assembly method. *Journal of Materials Chemistry* 2009, 19, 2006-2012.

42. Tu, M.; Sun, T.; Grattan, K., LSPR optical fibre sensors based on hollow gold nanostructures. *Sensors and Actuators B: Chemical* 2014, 191, 37-44.

43. Gowd, E. B.; Böhme, M.; Stamm, M. In *In situ GISAXS study on solvent vapour induced orientation switching in PS-b-P4VP block copolymer thin films*, *IOP Conference Series: Materials Science and Engineering*, 2010, 14, 012015. **DOI:** 10.1088/1757-899X/14/1/012015

44. van Zoelen, W.; Asumaa, T.; Ruokolainen, J.; Ikkala, O.; Ten Brinke, G., Phase behavior of solvent vapor annealed thin films of PS-b-P4VP (PDP) supramolecules. *Macromolecules* 2008, 41, 3199-3208.

45. Vyhnalkova, R.; Müller, A. H.; Eisenberg, A., Control of corona composition and morphology in aggregates of mixtures of ps-b-paa and ps-b-p4vp diblock copolymers: effects of ph and block length. *Langmuir* 2014, 30, 5031-5040.

46. Lazzari, M.; López-Quintela, M. A., Block copolymers as a tool for nanomaterial fabrication. *Advanced Materials* 2003, 15, 1583-1594.

47. Lodge, T. P., Block copolymers: past successes and future challenges. *Macromolecular chemistry and physics* 2003, 204, 265-273.

48. Lopes, W. A.; Jaeger, H. M., Hierarchical self-assembly of metal nanostructures on diblock copolymer scaffolds. *Nature* 2001, 414, 735-738.

49. Park, M.; Harrison, C.; Chaikin, P. M.; Register, R. A.; Adamson, D. H., Block copolymer lithography: periodic arrays of~ 1011 holes in 1 square centimeter. *Science* 1997, 276, 1401-1404.

50. Park, S.; Kim, B.; Wang, J. Y.; Russell, T. P., Fabrication of highly ordered silicon oxide dots and stripes from block copolymer thin films. *Advanced materials* 2008, 20, 681-685.

51. Zhu, H.; Lussier, F.; Ducrot, C.; Bourque, M.-J.; Spatz, J. P.; Cui, W.; Yu, L.; Peng, W.; Trudeau, L.-E.; Bazuin, C. G., Block copolymer brush layer-templated gold nanoparticles on nanofibers for surface-enhanced Raman scattering optophysiology. *ACS applied materials & interfaces* 2019.

52. Bastús, N. G.; Comenge, J.; Puntes, V., Kinetically controlled seeded growth synthesis of citrate-stabilized gold nanoparticles of up to 200 nm: size focusing versus Ostwald ripening. *Langmuir* 2011, 27, 11098-11105.

53. Martinsson, E.; Sepulveda, B.; Chen, P.; Elfwing, A.; Liedberg, B.; Aili, D., Optimizing the refractive index sensitivity of plasmonically coupled gold nanoparticles. *Plasmonics* 2014, 9, 773-780.

54. Ahamad, N.; Bottomley, A.; Ianoul, A., Optimizing refractive index sensitivity of supported silver nanocube monolayers. *The Journal of Physical Chemistry C* 2011, 116, 185-192.

55. Martinsson, E.; Otte, M. A.; Shahjamali, M. M.; Sepulveda, B.; Aili, D., Substrate effect on the refractive index sensitivity of silver nanoparticles. *The Journal of Physical Chemistry C* 2014, 118, 24680-24687.

56. Špačková, B.; Lebrušková, P.; Šípová, H.; Kwiecien, P.; Richter, I.; Homola, J., Ambiguous refractive index sensitivity of Fano resonance on an array of gold nanoparticles. *Plasmonics* 2014, 9, 729-735.

Table 1 Absorption spectra characteristics of AuNPs of different diameters in aqueous suspension (UV-vis, Figure S1) and assembled on optical fibers (LSPR, Figure 2a).

AuNP diameter (nm)	10	22	31	42	54	76	92
Resonance wavelength (UV-vis, nm)	520	523	525	529	533	546	560
Resonance wavelength (LSPR, nm)	553	575	586	618	630	682	715
FWHM (LSPR, nm)	54	66	62	59	65	98	124
Resonance depth (LSPR, %)	12	15	25	28	42	40	30

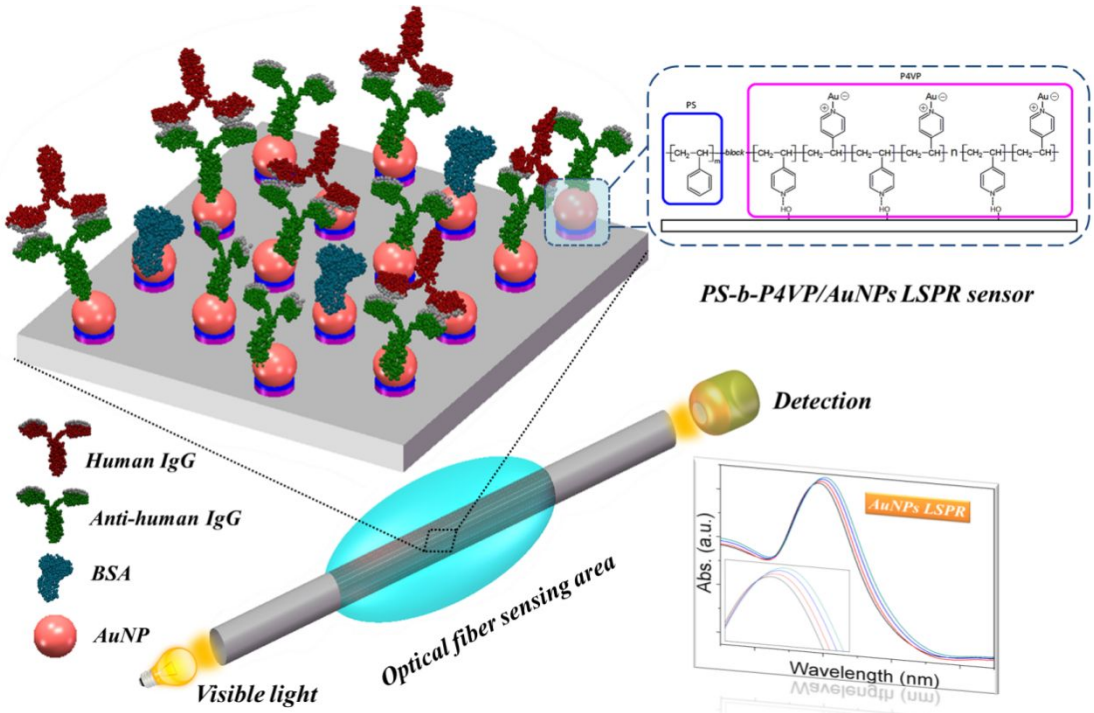

Figure 1. Schematic diagram of the optical fiber-based LSPR sensor.

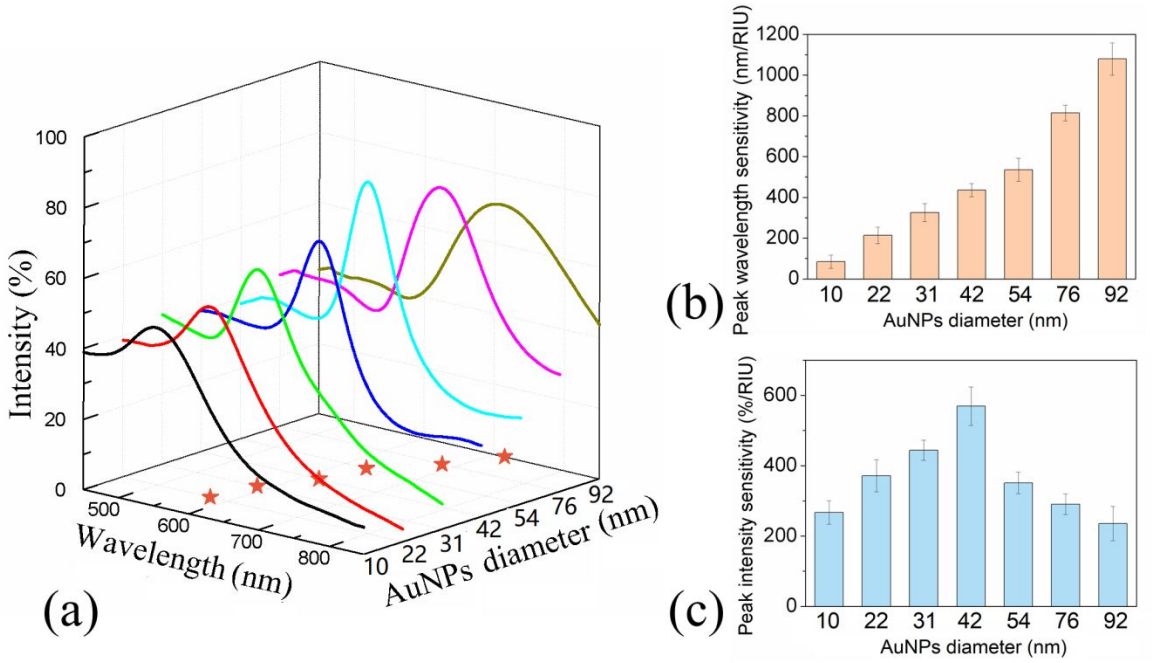

Figure 2. (a) Absorption spectra of AuNPs of different diameters in assembled films on optical fibers. The red stars indicate the wavelength of the LSPR peak maximum. Refractive index sensitivity of the LSPR peak (b) wavelength and (c) intensity for different particle diameters.

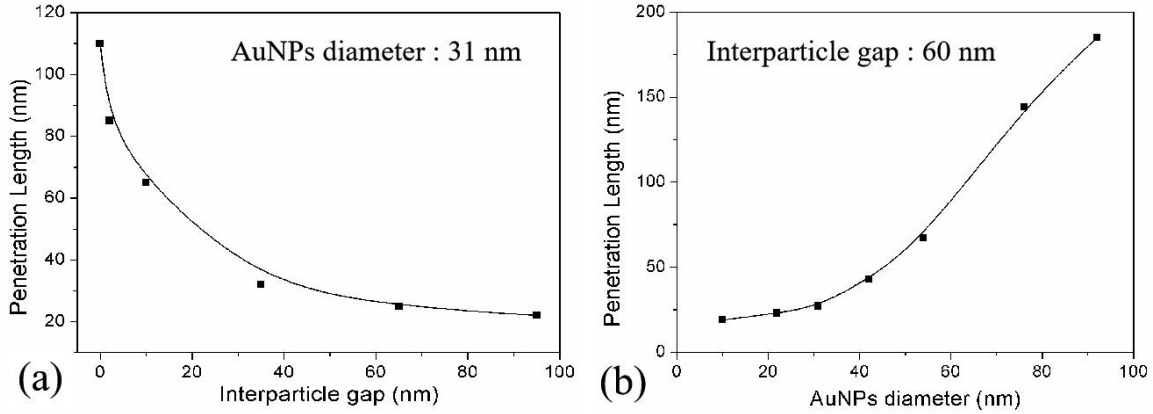

Figure 3. (a) Simulation results of the penetration depth in relation to the interparticle gap distance (the particle diameter was constant at 31 nm). (b) Simulation results of the penetration depth as a function of the nanoparticle size. The interparticle gap was constant at 60 nm.

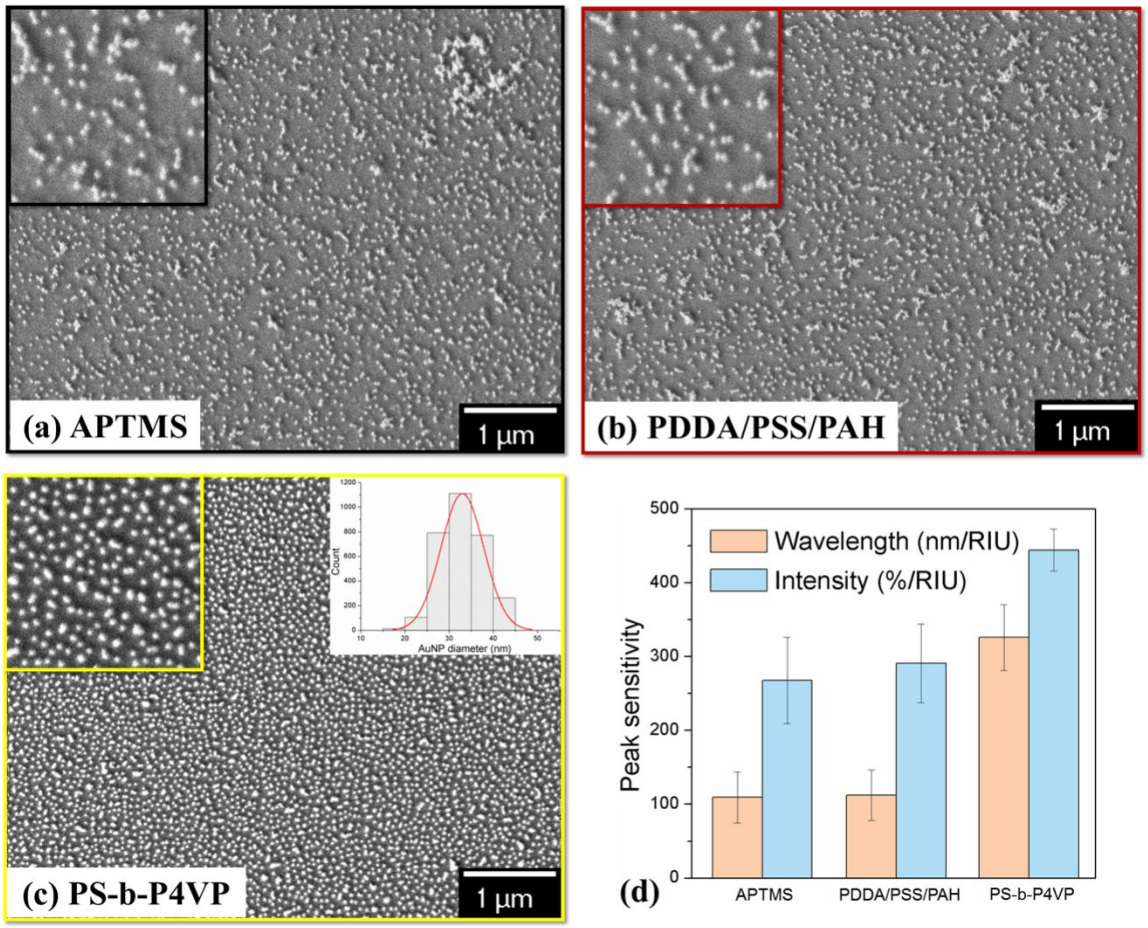

Figure 4. SEM images of AuNPs (31 nm in diameter) immobilized on optical fibers templated by (a) APTMS, (b) PDDA/PSS/PAH and (c) a PS-b-P4VP brush layer. (d) Refractive index sensitivity of the LSPR peak wavelength and intensity for the three AuNP deposition methods.

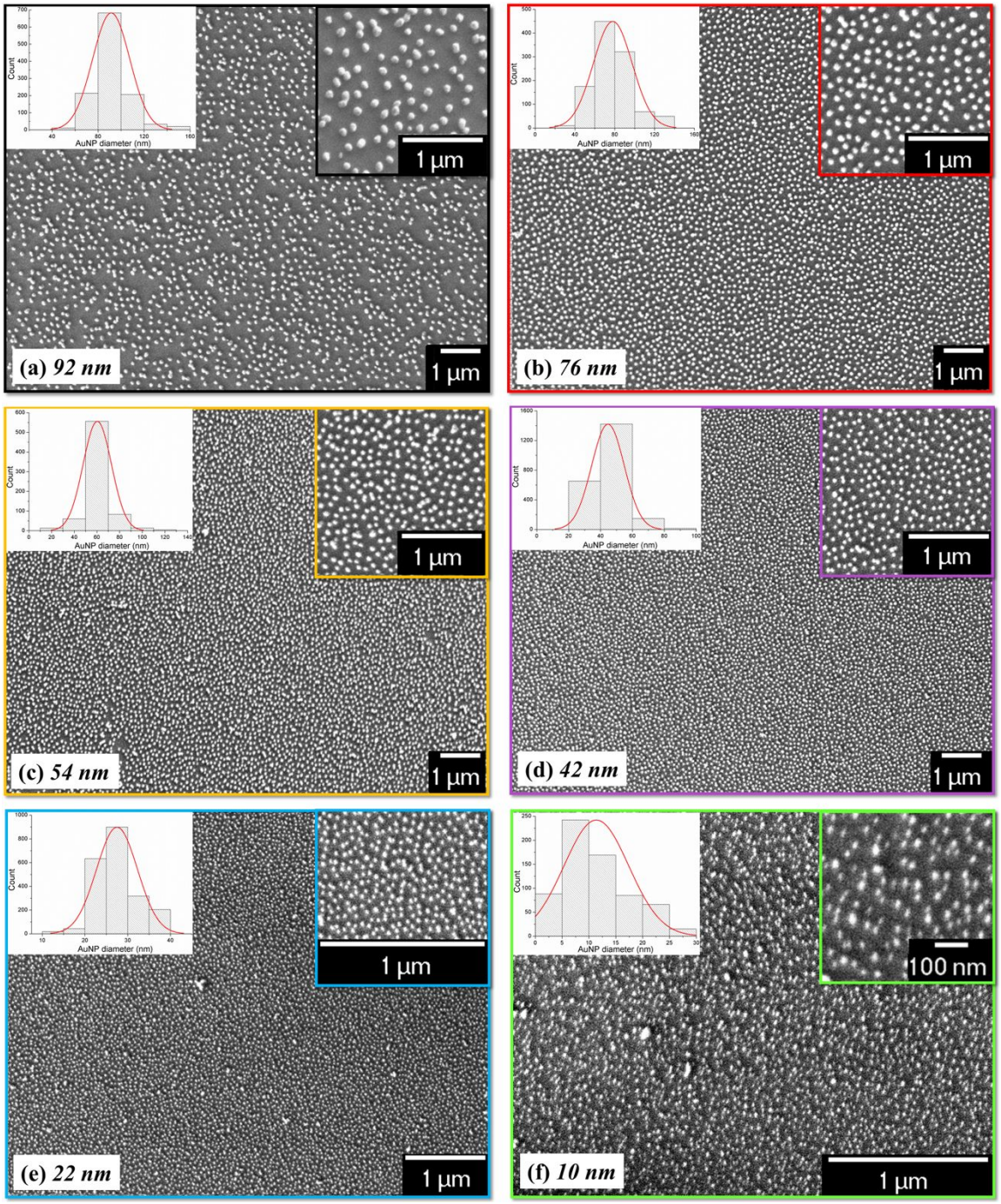

Figure 5. SEM images and diameter distributions of AuNPs of the average diameters specified in (a) to (f), deposited on PS-b-P4VP brush-templated optical fibers.

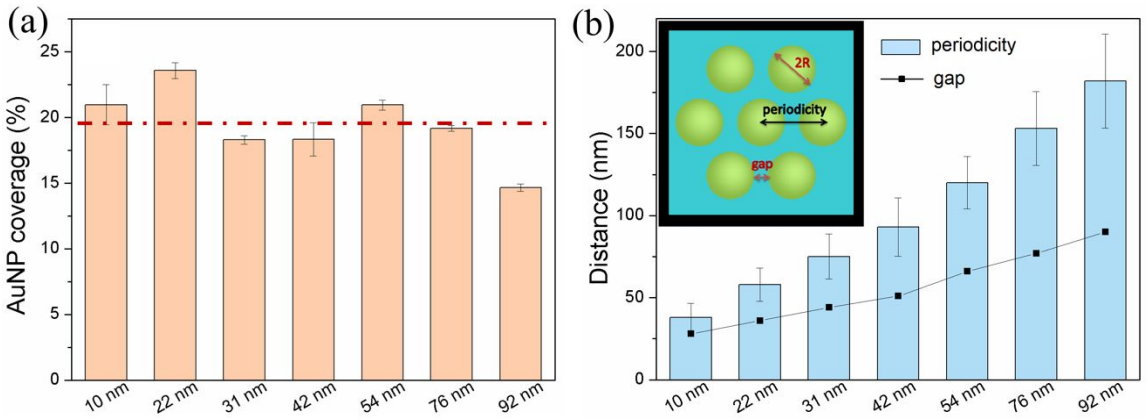

Figure 6. (a) Surface coverage by the AuNPs of different average diameters deposited on PS-b-P4VP brush-templated fibers. The red line represents the average coverage for the different particle sizes. (b) The average interparticle distances. The surface coverage and interparticle distances were calculated from Figure 4.

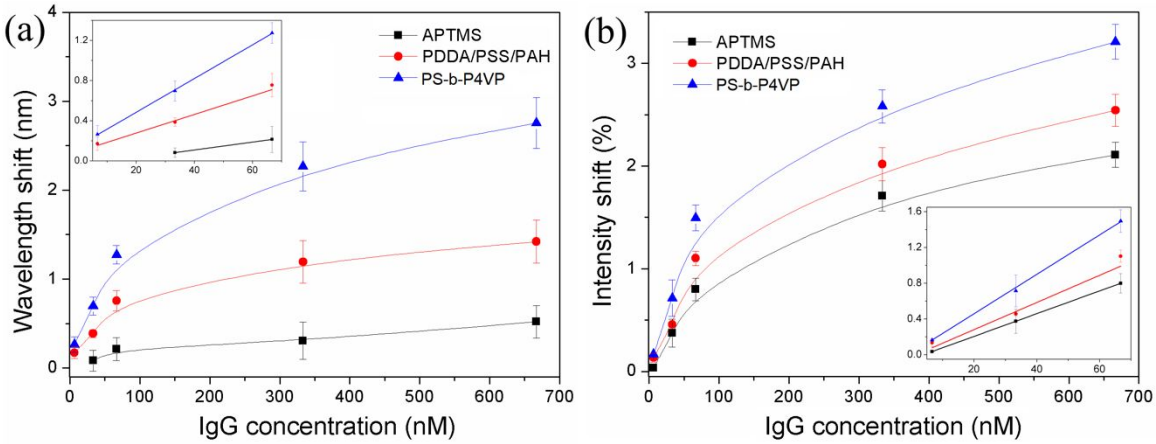

Figure 7. Calibrations curve of the LSPR peak (a) wavelength and (b) intensity as a function of human IgG concentration for three different AuNP deposition templates.

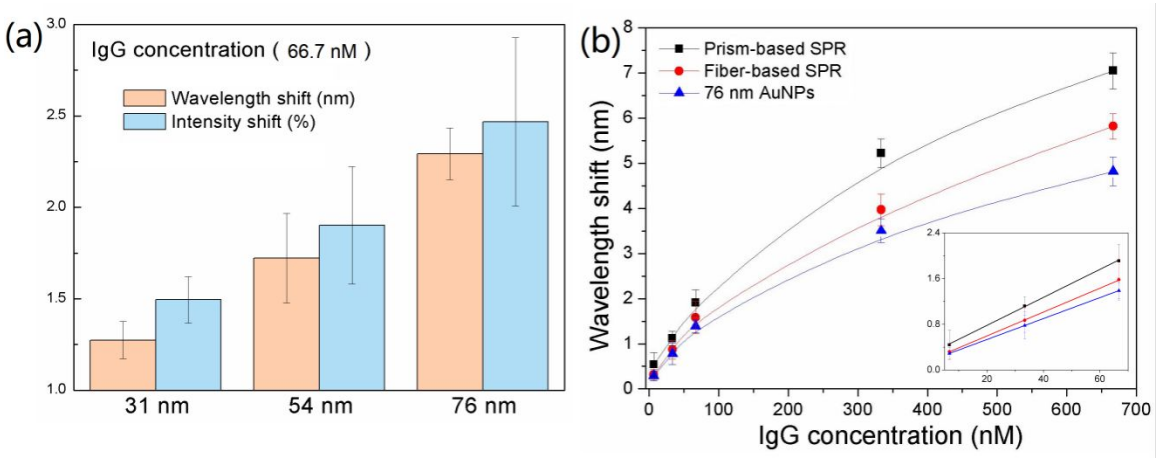

Figure 8. (a) LSPR peak wavelength and intensity shifts using different AuNP diameters for human IgG biosensing. The human IgG concentration was 66.7 nM. (b) Calibration curve for IgG using prism-based and fiber-based SPR sensors in identical conditions. Here, we used 76-nm AuNPs, which had the largest shift in Fig. 7(a), on a fiber-based LSPR sensor for comparison.

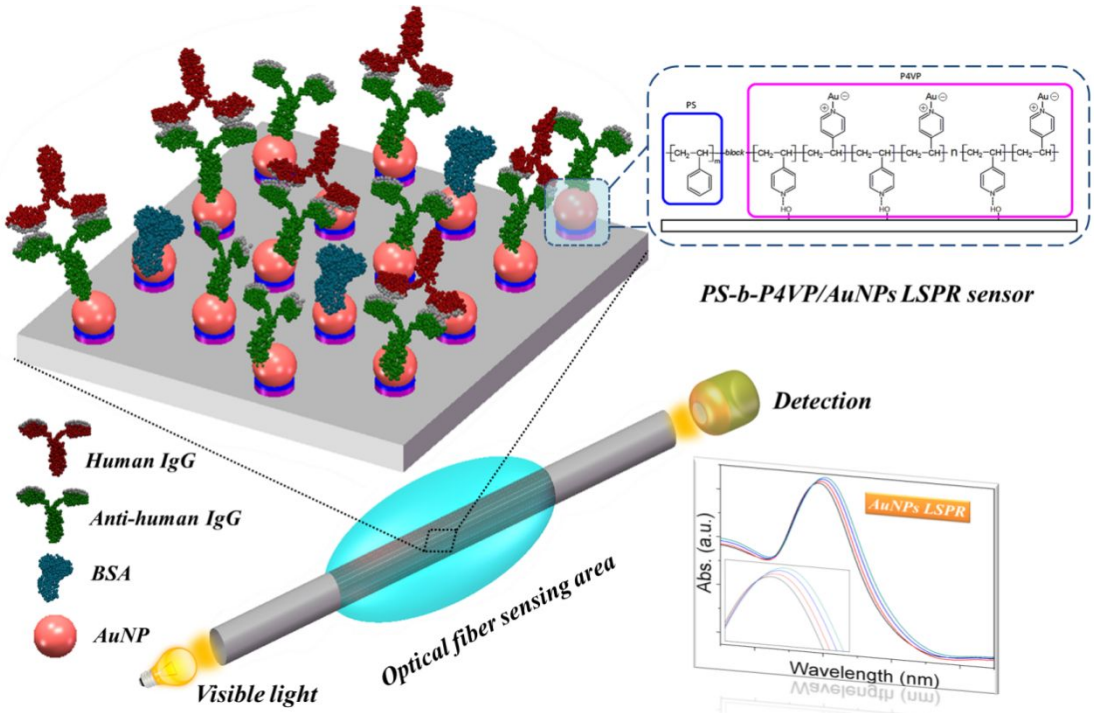
P4VP
PS
Au
PS-b-P4VP/AuNPs LSPR sensor
Detection
Human IgG
Anti-human IgG
BSA
AuNP
Optical fiber sensing area
Visible light
AuNPs LSPR
Abs. (a.u.)
Wavelength (nm)

For TOC only